Journal of Materials Chemistry C

ROYAL SOCIETY OF CHEMISTRY

PAPER

View Article Online
View Journal | View Issue

Open Access Article. Published on 08 August 2025. Downloaded on 10/26/2025 4:30:19 AM.
This article is licensed under a Creative Commons Attribution-NonCommercial 3.0 Unported Licence.

Check for updates

Cite this: J. Mater. Chem. C, 2025, 13, 18756

Phase stability of iron oxides epitaxial thin films under O_2, CO_2 and H_2O environmental conditions

Eugenia Sebastiani-Tofano, *[abc] Ana Garcia-Prieto[ab] and Juan Rubio-Zuazo *[ab]

Received 21st May 2025,
Accepted 30th July 2025

DOI: 10.1039/d5tc02013a

rsc.li/materials-c

The phase stability of iron oxide epitaxial thin films (FeO, Fe_3O_4, and γ-Fe_2O_3) under various environmental conditions, specifically O_2, H_2O and for the first time on CO_2, was systematically investigated using synchrotron based *in situ* grazing incidence X-ray diffraction (GIXRD) and reciprocal space mapping (RSM). We measured the phase transitions of these epitaxial thin films on $SrTiO_3$ (001) substrates at temperatures ranging from room temperature to 1100 °C, with gas pressures from 10^{-9} mbar to 1 bar. Our findings show that the phase stability of the films deviates from previously predicted phase diagrams, only available for O_2 and H_2O, particularly under low partial pressures, suggesting that the thin-film nature and substrate effects significantly influence the phase transitions. These findings highlight the complex interplay between temperature, gas pressure, and substrate role in determining and controlling the phase stability, providing a broader approach for phase engineering in complex oxide thin films.

1. Introduction

The technological potential of transition metal oxides relies heavily on the ability to control and stabilize their phases. Among these, iron oxides offer a variety of accessible phases (FeO, Fe_3O_4, γ-Fe_2O_3, α-Fe_2O_3, *etc.*) each with distinct magnetic, electronic, and catalytic properties. Their easy transformation between phases under temperature, gas pressure and overall chemical environment makes iron oxides suitable for a wide range of applications including spintronics, high-density data storage, energy harvesting, photoelectrochemical systems, and biomedical technologies.[1–9] Even more, using them in thin film form opens up new opportunities for technological advancements by allowing for precise control over the material's properties at the nanoscale and enhancing their performance in various applications.[4,6,9–12] Iron oxide thin films on oxide substrates are used in a broad range of devices because of their tuneable magnetic, electronic, and redox properties. For instance, Fe_3O_4 has been integrated into magnetic tunnel junctions (MTJs), showing tunnelling magnetoresistance at room temperature (RT).[13–15] Fe_3O_4 thin films and Fe/Fe_3O_4 bilayers have also been grown by chemical vapor deposition for spintronic device integration.[16] γ-Fe_2O_3 has been explored as a high-efficiency spin filtering material for spintronic devices.[17] Furthermore, Fe_3O_4 thin films exhibit resistive switching behaviour and electric-field-induced magnetization changes, offering potential for memory and logic applications.[18] Epitaxial Fe_3O_4 films also demonstrate multiferroic behaviour, combining ferroelectric and magnetic properties.[19,20] Beyond spintronics, iron oxides have also attracted significant attention in the field of solar energy. α-Fe_2O_3 has been extensively studied as a photoanode material for photoelectrochemical water splitting.[21] Redox cycling between Fe_3O_4 and FeO has been exploited in thermochemical processes for solar-driven hydrogen and syngas production.[22,23] Their integration in oxide heterostructures such as Fe_3O_4/$SrTiO_3$ also show emergent functionalities like magnetoelectric coupling and tuneable interfacial charge transfer.[9]

However, a key role remains on the preservation of the desired iron oxide phase under realistic environmental conditions, where substrate interactions and gas atmosphere play a defining role strongly affecting the phase stability. For example, magnetic tunnel junctions and spintronic devices using Fe_3O_4 often undergo post-deposition annealing in oxygen-deficient environments, where controlling temperature and partial pressure is crucial to preserve the Fe_3O_4 phase and avoid unwanted reduction to FeO or oxidation to γ-Fe_2O_3.[13,14,16] Resistive switching memory and logic devices exploit oxygen migration and redox changes in Fe_3O_4 thin films, making them sensitive to ambient oxygen content and thermal treatments.[18] In photoelectrochemical systems, α-Fe_2O_3 photoanodes are exposed to aqueous and CO_2-rich environments under illumination and heat, conditions that overlap with those simulated in our CO_2 and H_2O stability maps.[21,24] Thermochemical hydrogen production cycles based on FeO/Fe_3O_4 redox reactions operate at high temperatures and low oxygen partial pressures.[23]

[a] Spanish CRG BM25 Beamline SpLine at the ESRF, 71 avenue des Martyrs, 38000, Grenoble, France. E-mail: eugenia.sebastiani@esrf.fr, rubio@esrf.fr
[b] Instituto de Ciencia de Materiales de Madrid-ICMM/CSIC, Sor Juana Inés de la Cruz 3, Cantoblanco, 28049, Madrid, Spain
[c] Escuela de Doctorado UAM, Centro de Estudios de Posgrado, Universidad Autónoma de Madrid, Spain

 This journal is © The Royal Society of Chemistry 2025

Open Access Article. Published on 08 August 2025. Downloaded on 10/26/2025 4:30:19 AM.
This article is licensed under a Creative Commons Attribution-NonCommercial 3.0 Unported Licence.

These examples highlight the importance of synthesis and phase stabilization strategies on iron oxide thin films under elevated temperatures and high partial pressures of oxidizing gases. Specifically the understanding of the oxidation and reduction process is of special relevance. Nevertheless, the oxidation/reduction on iron oxides is a complex phenomenon that depends on many parameters and often diverges from predictions based on bulk oxide phase diagrams.[12,25,26] From a simple model, γ-Fe_2O_3 is prompt to be stabilized at high oxidation conditions, in contrary to FeO. Also, oxygen release/incorporation from the atomic structure strongly depends on the annealing temperature. Hence, the equilibrium of the oxygen stoichiometry on iron oxides will depend on a competitive oxidation/reduction effect based on the thermal and environmental conditions.

When these iron oxides are grown as epitaxial thin films on oxide substrates, the roll of the substrate such as oxygen free or deficient buffer must also be considered, as it can significantly influence the oxidation/reduction balance. This interaction further complicates the stability and phase transition of these oxides, driving a diverging behavior from that predicted for bulk materials. Genuzio *et al.*[26] observed that the transformations between the iron oxide phases occur differently depending on the substrate used as template for the growth, emphasizing the need to consider the substrate effect when studying the stability and phase transformations of iron oxide epitaxial thin films. They also found that, for annealing under oxygen environment, the phase transformations are not homogeneous but take place with conversion fronts that move at considerably different rates and with complicated morphologies depending on temperature and gas partial pressure.[26] Hamed *et al.*[12] also found that the phase transitions observed in ultrathin iron oxide films grown on Nb:$SrTiO_3$ and YSZ substrates differ significantly from the standard Fe_xO_y temperature–pressure phase diagrams. They demonstrate that in order to understand such deviations the total oxygen supply should be considered, including the oxygen provided by the oxide substrate, the oxygen already stored in the iron oxide film and the oxygen supplied by the external gas.

Such studies demonstrate the importance of understanding the phase stability of iron oxide thin films, and their interconversion.[12,26–30] However, there remains a gap in literature due to the small number of systematic studies aimed at constructing stability diagrams under different oxidative and reductive conditions. Comprehensive investigations into the phase stability of iron oxide epitaxial thin films under different atmospheres, such as O_2, CO_2, and H_2O, from UHV (reductive condition) to ambient pressure (oxidizing condition) are mandatory.

The present study shows a comprehensive investigation of the phase stability of iron oxides as epitaxial thin films under various environmental atmospheres and annealing temperatures. The phase transformation γ-Fe_2O_3/Fe_3O_4/FeO on epitaxial thin films grown by pulsed laser deposition (PLD) on $SrTiO_3$(001) and their stability was examined under different environmental conditions (temperature, gas, and partial pressure) using synchrotron based *in situ* grazing incidence X-ray diffraction (GIXRD)re. Stability phase diagrams are obtained in the annealing temperature range RT-1100 °C, under O_2, CO_2, and H_2O atmospheres with partial pressures between 10^{-9} mbar and 1 bar. Such research deepens our understanding of these versatile materials but also pave the way for their more effective use in various technological applications. Furthermore, while this study specifically addresses iron oxide epitaxial thin films on $SrTiO_3$ substrates, the concepts demonstrated here are broadly applicable to other complex oxide systems.

2. Experimental details

To study the behaviour of iron oxide thin films, we start from epitaxial γ-Fe_2O_3 and follow its transformation into Fe_3O_4 and FeO during thermal annealing in controlled gas atmospheres. We chose γ-Fe_2O_3 as the starting phase because it represents the most oxidized state among the iron oxides studied. Starting from this phase allows us to follow the full reduction through Fe_3O_4 and FeO under controlled thermal and environmental conditions by using *in situ* GIXRD and reciprocal space mapping (RSM) we track the environmental stability of the iron oxide phases in thin film form to build experimental stability phase diagrams. These diagrams reveal the stability regions of γ-Fe_2O_3, Fe_3O_4, and FeO as a function of annealing temperature and atmosphere (O_2, CO_2, H_2O) offering direct insight into how different phases emerge or disappear depending on the environment, under conditions that mimic real device environments.

In situ synchrotron based GIXRD was used to monitor the structural changes and phase stability of the epitaxial γ-Fe_2O_3 thin films under different environmental (annealing, gas and pressure) conditions. The experiments were conducted at the BM25-SpLine beamline at the ESRF[31–34] with a photon energy of 15 keV. The phase transformation was followed by *in situ* RSM and crystal truncation RODs (CTRs) in the temperature range RT-1100 °C and partial pressure range 10^{-9} mbar – 1 bar. O_2, CO_2, and H_2O gases were used. For the "low"-pressure regime (10^{-9} mbar to 10^{-4} mbar) the samples were mounted on a 2S + 3D diffractometer in horizontal geometry equipped with an ultra-high vacuum chamber.[31,32,34] Such an experimental set-up enables performing *in situ* measurements using different gasses from UHV to 10^{-4} mbar and at different annealing temperatures up to 1200 °C. For the "high"-pressure regime (1 mbar–1 bar) a domed Hot Stage cell from the Anton Paar company was used placed on a six-circle diffractometer in vertical geometry.[34] Such a set-up offers the possibility of performing a thermal treatment (from RT to 1100 °C) during *in situ* X-ray measurements (diffraction and spectroscopy) while introducing different gas atmospheres from 10^{-2} mbar to 1.5 bar. Both set-ups are installed at SpLine (BM-25). The XRD patters were acquired using a 2D detector which enables the acquisition of fast RSM and crystal truncation RODs (CTRs) with enough angular resolution and statistics to discriminate small shifts in the diffraction peaks, therefore allowing us to easily distinguish between the different oxide phases. For each gas (O_2, CO_2, and H_2O), a series of distinct partial pressures were set: for O_2 and CO_2, 10^{-8}, 10^{-6}, 10^{-4}, 1 mbar and 1 bar, and for H_2O, 10^{-8}, 10^{-6}, 10^{-4} and 20 mbar.

Open Access Article. Published on 08 August 2025. Downloaded on 10/26/2025 4:30:19 AM.
This article is licensed under a Creative Commons Attribution-NonCommercial 3.0 Unported Licence.

The annealing temperature was tuned in steps of 100 °C for each gas and partial pressure between RT and up to 1100 °C. The entire process was conducted in isobaric conditions, ensuring consistent pressure throughout each measurement for the different atmospheres. At each combination of temperature and partial pressure, a RSM was recorded around the (2 0 2) or the equivalent (0 −2 2) direction of the substrate to pinpoint the position of the iron oxide diffraction peak, allowing us the determination of the oxide phase.

Reference γ-Fe_2O_3, Fe_3O_4, and FeO epitaxial thin films were independently grown on $SrTiO_3$ (001) by PLD under optimized growth conditions to help with the phase identification during the *in situ* experiment. The PLD process for all the samples was carried out using a Nd:YAG laser with a wavelength of 355 nm, a frequency of 10 Hz, and an irradiance power of 1 J cm^{-2}. The base pressure of the chamber for the thin films deposition was 1×10^{-9} mbar. $5 \times 5 \times 0.5$ mm^3 substrates were used for all the depositions. The target to substrate distance was set to 50 mm and was vertically off-centred by 5 mm respect to the plume centre to ensure the substrate exposition to a vapour phase free of large particulates. All the ablation processes were performed with the substrates at an optimized temperature of 420 °C and with a varying oxygen partial pressure depending on the desired phase. Lower temperatures yielded a lack of crystallinity while at higher temperatures an island growth mode was obtained. For γ-Fe_2O_3 epitaxial thin films an oxygen partial pressure of 1×10^{-4} mbar ensured good oxygen stoichiometry, while for Fe_3O_4, and FeO the optimized partial pressure was 1×10^{-6} mbar. For the latest, a post annealing at 600 °C in UHV was necessary to achieve the single phase character. A polycrystalline Fe_2O_3 target was used revealing good iron and oxygen stoichiometry for all samples and references. The thin film quality (morphology, crystallinity and desired phase) was monitored by *in situ* reflection high-energy electron diffraction (RHEED) using a primary electron beam of 29 keV (see Fig. S2). Synchrotron based GIXRD was then used to verify the formation of single-phase films. The thicknesses of the layers were determined by low-angle X-ray reflectivity (Fig. S3).

3. Results and discussion

To demonstrate the ability to discriminate between the different iron oxide phases, GIXRD was performed on three reference epitaxial thin films (γ-Fe_2O_3, Fe_3O_4, and FeO) grown independently on $SrTiO_3$ (001) by PLD using optimized conditions. Fig. 1a shows the RSM obtained on the reference γ-Fe_2O_3, Fe_3O_4 and FeO thin films as an example. The substrate, $SrTiO_3$, has a

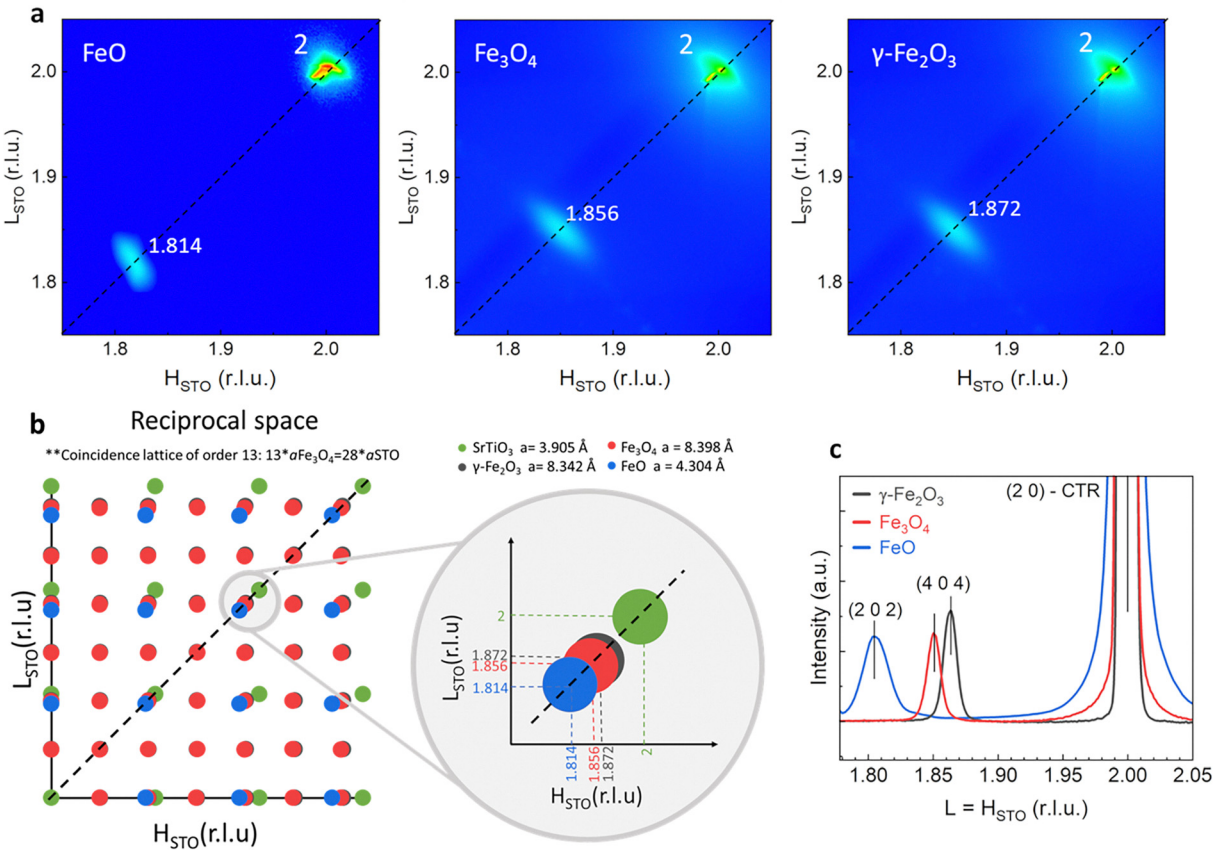

Fig. 1 (a) Representative RSM showing the diffraction peaks of reference FeO, Fe_3O_4, γ-Fe_2O_3 and $SrTiO_3$ (STO). (b) Schematic of reciprocal space illustrating the $SrTiO_3$, Fe_3O_4, γ-Fe_2O_3, and FeO lattices, and the alignment between them. (c) GIXRD linear scan obtained from the integration of the corresponding RSM of FeO, γ-Fe_2O_3, and Fe_3O_4 reference epitaxial thin films grown on $SrTiO_3$(001) substrates.

Open Access Article. Published on 08 August 2025. Downloaded on 10/26/2025 4:30:19 AM.
This article is licensed under a Creative Commons Attribution-NonCommercial 3.0 Unported Licence.

cubic structure with a lattice parameter of 3.905 Å. FeO, which also has a cubic structure with a bulk lattice parameter of 4.304 Å, grows fully relaxed in an axis-on-axis configuration with $SrTiO_3$. Within this model the FeO (202) diffraction peak is observed at $H = L = (3.905/4.304) \times 2 = 1.814$ in $SrTiO_3$ reciprocal lattice units for $K = 0$. Accordingly, relaxed Fe_3O_4 shows the corresponding (404) reflection at $H = (3.905/8.398) \times 4 = 1.856$, while γ-Fe_2O_3, with a relaxed bulk lattice parameter of 8.342 Å, shows the (404) reflection at $H = (3.905/8.342) \times 4 = 1.872$ in $SrTiO_3$ reciprocal lattice units. As the films grow relaxed maintaining a cubic lattice, the diffraction peaks are aligned in a straight line towards the origin in the H0L plane, as represented in the reciprocal space schema shown in Fig. 1b. From the corresponding RSM, the signal is then integrated to obtain a linear scan (Fig. 1c), showing the expected peaks shifting accordingly for all three oxides. The identification of only the FeO (202) reflection or the Fe_3O_4 or γ-Fe_2O_3 (404) reflection signifies the formation of single-phase films.[35,36]

Representative *in situ* GIXRD patterns as a function of the annealing temperature of iron oxide thin films on $SrTiO_3$ (001) substrates are shown on Fig. 2, illustrating typical results from the extensive range of diffraction measurements conducted. (See data availability section for the complete series of GIXRD scans across all conditions). The left panel shows patterns under ultra-high vacuum (UHV), while the right panel presents data at an oxygen partial pressure of 10^{-8} mbar. These patterns cover substrate temperatures from RT to 950 °C, denoted by the colour gradient. Vertical dashed lines act as visual guides for the expected peak positions of FeO, Fe_3O_4, and γ-Fe_2O_3 phases in $SrTiO_3$ reciprocal lattice units (r.l.u.). The variation in peak position with temperature offers insights into the phase transformation. It can be seen the evolution from γ-Fe_2O_3 to Fe_3O_4 at 440 °C for UHV conditions and a further reduction to FeO at 700 °C. In the 595 °C to 680 °C range Fe_3O_4 and FeO phases coexist with higher FeO/Fe_3O_4 ratio for higher temperatures. Upon insertion of 10^{-8} mbar of oxygen gas the phase transformation shifts to higher temperatures. Fe_3O_4 and FeO single phases are achieved at 625 °C and 860 °C, respectively. γ-Fe_2O_3 and Fe_3O_4 coexists in the temperature range between 450 and 590 °C, while Fe_3O_4 and FeO phases coexists between 720 and 830 °C. The phase transformation from maghemite to magnetite happens as Fe cations reduce their oxidation state from Fe^{3+} to Fe^{2+} simultaneously to a rearrangement of the iron and oxygen sites while conserving the inverse spinel crystal lattice. In maghemite, all iron atoms are Fe^{3+} and some octahedral sites are empty. In Fe_3O_4, both Fe^{2+} and Fe^{3+} are present in the octahedral sites, and all cation sites are occupied. As maghemite transforms into magnetite, oxygen is released, iron ions rearrange to fill the empty sites, and the lattice expands slightly because of the Fe^{2+} larger ionic radius. This change is reflected in the diffraction data as a shift of the (404) peak to lower H_{sto} values. Since the overall structure remains similar and the transformation is gradual, it is expected a smooth movement of the peak in the intermediate region rather than the appearance of two distinct phases, in accordance with our findings. This behaviour contrasts with the Fe_3O_4 to FeO transition, where the crystal structures are clearly different, and the coexistence of phases results in separate diffraction peaks. The temperature increase on the iron oxide phase reduction for slightly higher oxidizing conditions evidences the competitive effect between oxygen release and incorporation in the crystal lattice with the annealing temperature and oxidizing gas pressure.

It is worth noting that the profiles extracted from the RSMs obtained from GIXRD measurements (see Fig. S1 from the SI) show for the whole range of temperatures consistency in peak

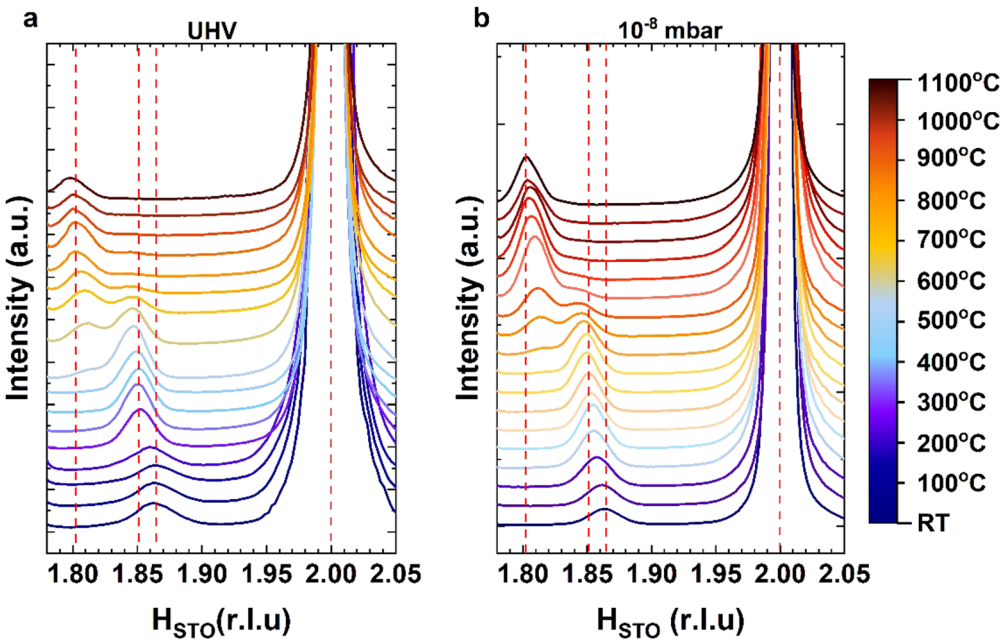

Fig. 2 Representative *in situ* GI-XRD patterns as a function of the annealing temperature for iron oxide thin films on STO (001) under ultra high vacuum (a) and oxygen partial pressure of 10^{-8} mbar of O_2 (b). Red straight dashed lines help point out where the FeO, Fe_3O_4, and γ-Fe_2O_3, peaks are expected.

Open Access Article. Published on 08 August 2025. Downloaded on 10/26/2025 4:30:19 AM.
This article is licensed under a Creative Commons Attribution-NonCommercial 3.0 Unported Licence.

intensity and position along both the in-plane (H and K) and out-of-plane (L) directions, indicating that the thin film undergoes symmetrical deformation in all directions maintaining its cubic structure across the temperature range studied.

The obtained phase diagram for iron oxide films grown on $SrTiO_3$(001) substrates are presented in Fig. 3, under (a) O_2, (b) CO_2 and (c) H_2O. The stability regions of the iron oxide phases are detailed as determined by *in situ* GIXRD. The phase stability regions are color-coded: the blue, red, and grey areas represent the stability regions for FeO, Fe_3O_4, and γ-Fe_2O_3, respectively. Dark blue and dark red areas represent FeO/Fe_3O_4 and Fe_3O_4/γ-Fe_2O_3 phase coexistence, respectively.

FeO is stable at low partial pressures and high temperatures, allowing the equilibrium between oxygen release due to the high temperature and the oxygen incorporation due to the oxidizing atmosphere. Under oxygen atmosphere, FeO is only stable at very low partial pressures (between 10^{-9} and 10^{-6} mbar) and temperature range 600 °C (for 10^{-9} mbar) to 1200 °C (for 10^{-6} mbar). Under CO_2 and H_2O, due to their lower oxidizing capability as compared to O_2, the pressure range is enlarged up to 10^{-5} mbar and 10^{-2} mbar, respectively, for equivalent high temperature values.

Fe_3O_4 is stable over a narrow window of intermediate pressures and temperatures, making it particularly sensitive to environmental conditions. Under an oxygen atmosphere, Fe_3O_4 is stable at 500 °C for a partial pressure of 10^{-8} mbar. Temperatures in the 800 to 1100 °C are needed for 10^{-5} mbar O_2 partial pressure.

Under CO_2, Fe_3O_4 is stabilized at high-pressure values (mbar) for temperatures above 800 °C. At such pressures, Fe_3O_4 is only stable for H_2O at very high temperatures (1200 °C). Compared to the broader stability ranges of FeO and γ-Fe_2O_3, the narrow window for Fe_3O_4 highlights how difficult it is to preserve this phase and how challenging it can be to synthesise and integrate in other devices. Even though many device applications operate at RT conditions, the fabrication and post-processing steps often involve elevated temperatures and controlled environments. Understanding this narrow stability window not only helps preserve its properties during synthesis but also ensure long-term integrity given by the post-processing conditions.

In the other hand, γ-Fe_2O_3 is stable at higher partial pressures and lower temperatures compared to FeO and Fe_3O_4. In an oxygen atmosphere, at very low pressure, γ-Fe_2O_3 is only stable at temperatures below 300 °C. As the partial pressure is increased up to 10^{-2} mbar, the phase stability temperature increases up to 1200 °C. For higher O_2 pressures, the γ-Fe_2O_3 is stable for the complete temperature range used in this work. Under CO_2, the temperature dependence of the phase stability with the partial gas pressure is very flat. γ-Fe_2O_3 is stable for temperatures below 300 °C at very low CO_2 partial pressures and below 500 °C for high partial pressures. A similar behaviour is obtained for H_2O atmosphere, except for partial pressures above 10^{-2} mbar for which the temperature increases monotonically up to 750 °C for a partial pressure of 20 mbar.

When comparing the three diagrams, it is evident that O_2 is the most oxidizing atmosphere as evidenced by the wider temperature range for the stability of γ-Fe_2O_3 in comparison to H_2O and CO_2. For partial pressures below 10^{-3}mbar, the CO_2 is more oxidizing than H_2O as evidenced by the wider temperature range for Fe_3O_4 stabilization and the narrower temperature range for FeO stabilization. However, at partial pressures above

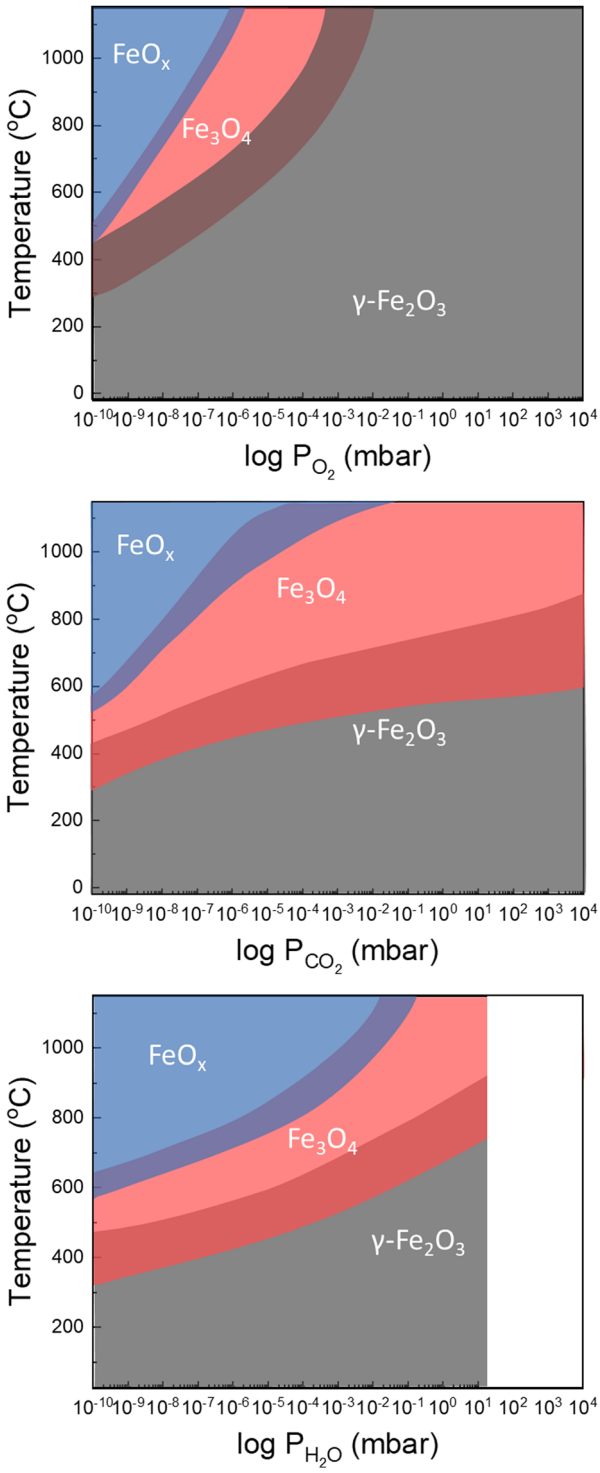

Fig. 3 Phase diagram of iron oxide films on $SrTiO_3$(001) substrates under varying (top) O_2, (middle) CO_2 and (bottom) H_2O partial pressures and temperatures. The experimental stability regions for FeO, Fe_3O_4 and γ-Fe_2O_3 are represented by the blue, red and grey areas. Dark blue and red areas represent FeO/Fe_3O_4 and Fe_3O_4/γ-Fe_2O_3 coexistence, respectively.

Open Access Article. Published on 08 August 2025. Downloaded on 10/26/2025 4:30:19 AM.
This article is licensed under a Creative Commons Attribution-NonCommercial 3.0 Unported Licence.

10^{-3} mbar, H_2O is more oxidizing than CO_2 as shown by the wider temperature range for γ-Fe_2O_3 stabilization.

The obtained experimental diagrams differ from the calculated temperature–pressure phase diagram for the iron oxygen system presented by G. Ketteler *et al.*[29] for O_2 and H_2O. Our findings demonstrate that for O_2 low partial pressures the transformation between oxides happens at lower temperatures than predicted by the calculations, especially for the Fe_3O_4–FeO transformation. Concerning the Fe_3O_4–Fe_2O_3 transformation a more relevant temperature dependence with the O_2 pressure has been obtained experimentally. The transition temperature increases rapidly with the gas partial pressure increase, contrary to the calculations. A similar behaviour is obtained for H_2O atmosphere. Lower temperatures are obtained experimentally for the stability of FeO at very low H_2O pressure. In addition, FeO remains stable for a larger H_2O pressure range. However, the Fe_3O_4–Fe_2O_3 transition behaviour with temperature and pressure under H_2O is in accordance with the calculations.

The observed discrepancies, especially for the low-pressure range, can be ascribed to the thin epitaxial character of the present films as compared to the stand-alone system used for the calculations. Also, the role of the substrate, specifically $SrTiO_3$, needs to be considered, since it acts as an oxygen buffer. Genuzio *et al.*[26] noted that the $SrTiO_3$ substrate contributes additional oxygen, significantly affecting the oxidation/reduction balance and altering the phase stability regions. This release of oxygen from the $SrTiO_3$ substrate was observed by Arnay *et al.*,[37] who noted that high-temperature thermal treatments lead to the release of oxygen, which begins at temperatures of 700 °C under reductive conditions. It should be noted that even in an externally oxidizing atmosphere, only a portion of that oxygen actually diffuses all the way through the iron oxide film to reach the substrate. In other words, the thin film itself absorbs most of the oxygen, acting as a partial barrier and causing the substrate to remain in a more reduced state than expected under purely oxidizing conditions. Any oxygen released from the substrate is directly taken up by the iron

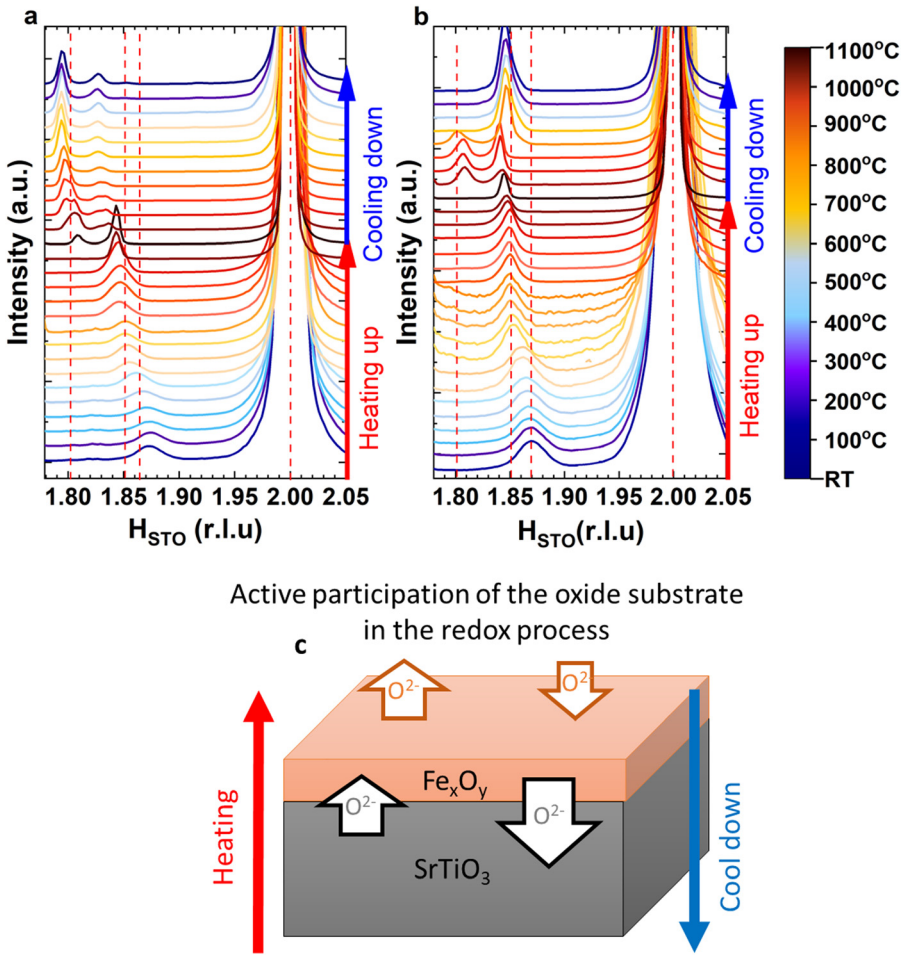

Fig. 4 GIXRD intensity profiles in an atmosphere of 10^{-6} mbar of (a) CO_2 and (b) O_2 as a function of temperature during heating and cooling processes. (c) Role of the STO substrate, contributing with additional oxygen and significantly impacting the oxidation/reduction balance and phase stability regions. At high temperatures, the STO substrate releases oxygen, creating vacancies and altering the effective oxygen pressure within the film. During cooling, the substrate reabsorbs oxygen, reducing the thin film. Once the substrate recuperates the oxygen stoichiometry, the film can re-oxidate from the oxidizing atmosphere.

Open Access Article. Published on 08 August 2025. Downloaded on 10/26/2025 4:30:19 AM.
This article is licensed under a Creative Commons Attribution-NonCommercial 3.0 Unported Licence.

oxide layer, raising its effective oxidation state. Meanwhile, the substrate compensates by creating oxygen vacancies within its own lattice, leading to a non-equilibrium configuration. Later, as temperatures shift or conditions change, the substrate naturally seeks to fill these vacancies by taking the oxygen back from the film leaving it in a more reduced state. Such a competitive process will depend on the annealing temperature and on the substrate used. During heating up the release of oxygen from the substrate is more favourable, while the opposite will happen during the cooling down process. This effect is shown in Fig. 4, as an example, for a CO_2 and O_2 atmosphere at 10^{-6} mbar. The substrate initially releases oxygen at high temperatures, preventing the formation of FeO. During the cooling down process, the $SrTiO_3$ substrate absorbs oxygen from the thin film, reducing it to form FeO. Once the substrate recovers the oxygen stoichiometry, the thin film starts to re-oxidize to Fe_3O_4 from the oxidizing atmosphere. This behaviour is consistently observed across different atmospheres, demonstrating the active participation of the oxide substrate in the redox process. This demonstrates that substrate oxygen exchange must be considered when designing functional oxide thin films for real operating environments such as spintronic devices, resistive switching memory, environmental sensors, or high-temperature energy conversion systems, where the interplay between redox processes and structural stability is critical for performance and durability.

It is important to note that the overall response of the system to the phase stability depends on the morphology of the thin films. For instance, films grown at different pressures or temperatures will show a different morphology scenario. Specifically an island growth mode is obtained when deposition is performed at higher temperatures and higher oxygen pressure. It is expected that such an island formation will modify considerably the redox activity due to the modification of the crystallographic orientation, the increase of surface area and the release of epitaxial strain. Although all these factors can potentially increase the redox activity of the system, it will be on detrimental of the engineering control. This behaviour can be extrapolated to other oxides based on transition metals in which the growth conditions not only affect to the oxide phase but also to the thin film morphology.

4. Conclusions

This study provides phase stability diagrams of iron oxides (FeO, Fe_3O_4, and γ-Fe_2O_3) epitaxial thin films grown on $SrTiO_3$ (001) substrates under O_2, H_2O and for the first time on CO_2 atmospheres in the temperature range RT-1100 °C and pressure range 10^{-9} mbar – 1 bar. Our findings show that O_2 is the most oxidizing gas, in comparison to CO_2 and H_2O, for which FeO is only stable at very low ratio of partial pressure to temperature, while Fe_3O_4 and y-Fe_2O_3 are stable at intermediate and high ratios, respectively. For partial pressures below 10^{-3} mbar, the CO_2 is more oxidizing than H_2O. In this pressure range FeO is only stable at very low ratios for CO_2 while extends to intermediate ratios for H_2O. y-Fe_2O_3 is only stable at low temperatures for both atmospheres, while Fe_3O_4 is stable at moderate temperatures for H_2O and moderate-to-high temperatures for CO_2. However, at partial pressures above 10^{-3} mbar, H_2O is more oxidizing than CO_2 as revealed by the wider temperature range for γ-Fe_2O_3 stabilization. Our results also show significant deviations from the calculated phase diagrams, only available for O_2 and H_2O, especially under low partial pressures, where phase transitions occur at lower temperatures than predicted. These discrepancies are attributed to the unique thin-film nature and the role of the $SrTiO_3$ substrate, which acts as an oxygen buffer, influencing the oxidation/reduction processes and altering the phase stability. These observations are relevant for a better understanding of the behaviour of these thin films and highlight the need to consider the substrate effects and environmental conditions when designing iron oxide thin films for practical applications, where the behaviour can diverge significantly from traditional models based on bulk materials.

Author contributions

The manuscript was written through contributions of all authors. All authors have given approval to the final version of the manuscript. E. Sebastiani-Tofano: conceptualization, methodology, investigation, data curation, formal analysis, visualization, writing – original draft, writing – review and editing. J. Rubio-Zuazo: conceptualization, methodology, investigation, visualization, validation, writing – review and editing, supervision, resources, project administration. A. Garcia-Prieto: scientific discussions, writing – review and editing.

Conflicts of interest

There are no conflicts to declare.

Data availability

The datasets supporting the findings of this study, including the integrated GIXRD scans used to construct Fig. S2, S3 and S4, are available in the Digital. CSIC repository at: **https://doi.org/10.20350/digitalCSIC/17500**.

Supplementary information is available. Additional structural characterization data for the γ-Fe_2O_3 thin films discussed in this work. A representative set of GIXRD intensity profiles in the in-plane and out-of-plane directions at 1 mbar CO_2, an in situ RHEED pattern of the γ-Fe_2O_3 thin films grown on STO(001) and low-angle XRR measurements demonstrating the smooth surfaces and layer-by-layer epitaxial growth and confirming the film thickness. See DOI: **https://doi.org/10.1039/d5tc02013a**

Acknowledgements

The authors are grateful to the SpLine staff for their valuable help and for the financial support from the Spanish Ministerio

Open Access Article. Published on 08 August 2025. Downloaded on 10/26/2025 4:30:19 AM.
This article is licensed under a Creative Commons Attribution-NonCommercial 3.0 Unported Licence.

de Ciencia, Innovacion y Universidades and Consejo Superior de Investigaciones Cientificas under Grant no. 2010 6O E 013 and 2021 60 E 030.

References

1 E. Acha, J. Requies, M. B. Güemez, V. L. Barrio, J. F. Cambra and P. L. Arias, *Int. J. Hydrogen Energy*, 2014, **39**, 5257–5266.
2 M. dos Santos Pires, L. C. Tavares Lacerda, S. Corrêa, T. Cardoso Silva, A. Alves de Castro and T. C. Ramalho, in *Recent Advances in Complex Functional Materials: From Design to Application*, ed. E. Longo and F. De Almeida la Porta, Springer, Cham, 2017, pp. 409–425.
3 H. Tokoro, A. Namai and S. I. Ohkoshi, *Dalton Trans.*, 2021, **50**, 452–459.
4 A. Osaka, D. Toh, K. Yamauchi, K. Hattori, X. Shi, F. Guo, H. Tanaka and A. N. Hattori, *ACS Appl. Nano Mater.*, 2021, **4**, 12091–12097.
5 S. A. Siddiqui, D. Hong, J. E. Pearson and A. Hoffmann, *Coatings*, 2021, **11**, 786.
6 A. Hamie, Y. Dumont, E. Popova, A. Fouchet, B. Warot-Fonrose, C. Gatel, E. Chikoidze, J. Scola, B. Berini and N. Keller, *Thin Solid Films*, 2012, **525**, 115–120.
7 A. V. Ramos, J.-B. Moussy, M.-J. Guittet, A. M. Bataille, M. Gautier-Soyer, M. Viret, C. Gatel, P. Bayle-Guillemaud and E. Snoeck, *J. Appl. Phys.*, 2006, **100**, 103902.
8 P. Tartaj, M. P. Morales, T. Gonzalez-Carreño, S. Veintemillas-Verdaguer and C. J. Serna, *Adv. Mater.*, 2011, **23**, 5243–5249.
9 M. H. Hamed, R. A. Hinz, P. Lömker, M. Wilhelm, A. Gloskovskii, P. Bencok, C. Schmitz-Antoniak, H. Elnaggar, C. M. Schneider and M. Müller, *ACS Appl. Mater. Interfaces*, 2019, **11**, 7576–7583.
10 B. Cheng, X. Liu and J. Hu, *Micro Nanostruct.*, 2022, **167**, 107183.
11 P. Kumar, H. No-Lee and R. Kumar, *J. Mater. Sci.: Mater. Electron.*, 2014, **25**, 4553–4561.
12 M. H. Hamed, D. N. Mueller and M. Müller, *J. Mater. Chem. C*, 2020, **8**, 1335–1343.
13 K. S. Yoon, J. Hyun Koo, Y. Ho Do, K. Woong Kim, C. Ok Kim and J. Pyo Hong, *J. Magn. Magn. Mater.*, 2005, **285**, 125–129.
14 T. Kado, *Appl. Phys. Lett.*, 2008, **92**, 092502.
15 T. Nagahama, Y. Matsuda, K. Tate, T. Kawai, N. Takahashi, S. Hiratani, Y. Watanabe, T. Yanase and T. Shimada, *Appl. Phys. Lett.*, 2014, **105**, 102410.
16 S. Vangelista, R. Mantovan, S. Cocco, A. Lamperti, O. Salicio and M. Fanciulli, *Thin Solid Films*, 2012, **520**, 4617–4621.
17 P. Li, C. Xia, Z. Zhu, Y. Wen, Q. Zhang, H. N. Alshareef and X. X. Zhang, *Adv. Funct. Mater.*, 2016, **26**, 5679–5689.
18 J. Ren, J. Li, S. Zhang, J. Li, W. Su, D. Wang, Q. Cao and Y. Du, *J. Magn. Magn. Mater.*, 2021, **538**, 168265.
19 M. Alexe, M. Ziese, D. Hesse, P. Esquinazi, K. Yamauchi, T. Fukushima, S. Picozzi and U. Gösele, *Adv. Mater.*, 2009, **21**, 4452–4455.
20 J. López-Sánchez, A. Del Campo, A. Quesada, A. Rivelles, M. Abuín, R. Sainz, E. Sebastiani-Tofano, J. Rubio-Zuazo, D. A. Ochoa, J. F. Fernández, J. E. García and F. Rubio-Marcos, *ACS Appl. Mater. Interfaces*, 2024, **16**, 19866–19876.
21 K. Sivula, F. Le Formal and M. Grätzel, *ChemSusChem*, 2011, **4**, 432–449.
22 G. L. Bachirou, Y. Shuai, J. Zhang, X. Huang, Y. Yuan and H. Tan, *Int. J. Hydrogen Energy*, 2016, **41**, 19936–19946.
23 A. Statmatiou, P. Loutzenhiser and A. Steinfeld, *Chem. Mater.*, 2010, **22**, 851–859.
24 L. Liccardo, E. Lushaj, L. Dal Compare, E. Moretti and A. Vomiero, *Small Sci.*, 2022, **2**, 2100104.
25 M. Ritter and W. Weiss, *Surf. Sci.*, 1999, **432**, 81–94.
26 F. Genuzio, A. Sala, T. Schmidt, D. Menzel and H. J. Freund, *J. Phys. Chem. C*, 2014, **118**, 29068–29076.
27 F. Genuzio, A. Sala, T. Schmidt, D. Menzel and H. J. Freund, *Surf. Sci.*, 2016, **648**, 177–187.
28 K. Freindl, J. Wojas, N. Kwiatek, J. Korecki and N. Spiridis, *J. Chem. Phys.*, 2020, **152**, 054701.
29 G. Ketteler, W. Weiss, W. Ranke and R. Schlögl, *Phys. Chem. Chem. Phys.*, 2011, **3**, 1114–1122.
30 M. Stir, K. Ishizaki, S. Vaucher and R. Nicula, *J. Appl. Phys.*, 2009, **105**, 124901.
31 J. Rubio-Zuazo, M. Escher, M. Merkel and G. R. Castro, *Rev. Sci. Instrum.*, 2010, **81**, 043304.
32 J. Rubio-Zuazo and G. R. Castro, *J. Vac. Sci. Technol., A*, 2013, **31**, 031103.
33 J. Rubio-Zuazo, P. Ferrer, A. López, A. Gutiérrez-León, I. da Silva and G. R. Castro, *Nucl. Instrum. Methods Phys. Res., Sect. A*, 2013, **716**, 23–28.
34 J. Rubio-Zuazo and G. R. Castro, *Nucl. Instrum. Methods Phys. Res., Sect. A*, 2005, **547**, 64–72.
35 J. Rubio-Zuazo, A. Chainani, M. Taguchichi, D. Malterre, A. Serrano and G. R. Castro, *Phys. Rev. B*, 2018, **97**, 235148.
36 J. Rubio-Zuazo, L. Onandia, E. Salas-Colera, A. Muñoz-Noval and G. R. Castro, *J. Phys. Chem. C*, 2015, **119**, 1108–1112.
37 I. Arnay, J. Rubio-Zuazo and G. R. Castro, *Appl. Surf. Sci.*, 2018, **427**, 561–565.